PAPER

Check for updates

Thermophysical properties of lithium thiogallate that are important for optical applications†

Alexey Kurus, [ID] [ab] Alexander Yelisseyev, [ab] Sergei Lobanov, [ab] Pavel Plyusnin, [ID] [c] Maxim Molokeev, [de] Leonid Solovyev, [f] Dmitry Samoshkin, [g] Sergei Stankus, [g] Svetlana Melnikova [d] and Lyudmila Isaenko [ID] [ab]

Lithium thiogallate LiGaS$_2$ is one of the most common nonlinear crystals for mid-IR due to its extreme beam strength and wide transparency range; however, its thermophysical properties have not yet been practically studied. Large crystals of high optical quality are grown. DTA revealed features at 1224 K below melting point (1304 K) that are associated with the oxygen containing compounds of the LiGaO$_{2-x}$S$_x$ type. The thermal conductivity of LiGaS$_2$ (about 10.05 W (m^{-1} K^{-1})) and band gap value (3.93 eV at 300 K) are found to be the highest in the LiBC$_2$ family. Isotropic points in the dispersion characteristics for the refractive index are found and LiGaS$_2$-based narrow-band optical filters, smoothly tunable with temperature changes, are demonstrated. Intense blue photoluminescence of anionic vacancies V_S is observed at room temperature after annealing LiGaS$_2$ in vacuum, whereas orange low-temperature emission is related to self-trapped excitons. When LiGaS$_2$ crystals are heated, spontaneous luminescence (pyroluminescence) takes place, or thermoluminescence after preliminary UV excitation; the parameters of traps of charge carriers are estimated. The obtained data confirm the high optical stability of this material and open up prospects for the creation of new optical devices based on LiGaS$_2$.

1. Introduction

Modern science and technology urgently require mid-infrared (mid-IR) lasers for applications in, *e.g.*, IR remote communications, environment monitoring and sensing, and organic tissue imaging.[1] The simplest way to obtain tunable coherent radiation in the middle infrared (mid-IR) is the nonlinear converting of the radiation of an all-solid-state laser emitting in the near IR (for example, at 1.06 μm) with optical parametric oscillation (OPO) or differential frequency generation (DFG) processes.[1]

ᵃNovosibirsk State University, 2 Pirogov str., Novosibirsk, 630090, Russia. E-mail: kurusaf@igm.nsc.ru

ᵇSobolev Institute of Geology and Mineralogy SB RAS, 3 Kopyug ave., Novosibirsk, 630090, Russia

ᶜNikolaev Institute of Inorganic Chemistry SB RAS, 3 Lavrentyev ave., Novosibirsk, 630090, Russia

ᵈKirensky Institute of Physics SB RAS, Krasnoyarsk, 660036, Russia

ᵉSiberian Federal University, Krasnoyarsk 660041, Russia

ᶠInstitute of Chemistry and Chemical Technology SB RAS, 42 K. Marx str., Krasnoyarsk, 66049, Russia

ᵍKutateladze Institute of Thermophysics SB RAS, 1 Lavrentyev ave., Novosibirsk, 630090, Russia

† Electronic supplementary information (ESI) available: Difference Rietveld plot of LiGaS$_2$ (Fig. S1) and tables with fractional atomic coordinates and isotropic displacement parameters (Table S1) and main bond lengths of LiGaS$_2$ (Table S2) are given in the ESI. Comparison of the X-ray diffractograms for LiGaS$_2$ obtained at 1080 K (above) and LiGaO$_2$ is given in Fig. 2S. See DOI: 10.1039/d1ra05698k
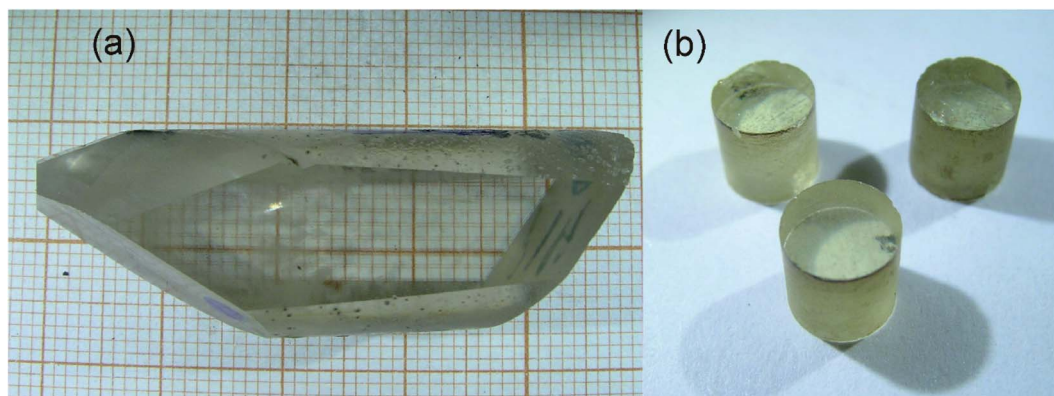
The main requirements for a nonlinear optical crystal are: transparency in a wide wavelength range (I), high second-order nonlinear susceptibility (II), high optical damage threshold (LDT, III), sufficiently high birefringence $\Delta n \sim (0.03–0.10)$ (IV), and the possibility of obtaining large crystals (V).[2,3] Note that the simultaneous satisfaction of all above conditions is an enormous challenge because some of them are contradictory. For a long time, only a few crystals met most of these requirements to some extent and were commercially available: silver thiogallate and selenogallate (AgGaS$_2$ and AgGaSe$_2$), as well as ZnGeP$_2$. In the last decade, much attention has also been paid to lithium-containing ternary chalcogenides of the LiBC$_2$ family, where B = In, Ga, and C=S, Se, Te.[2,4,5] It is established that the main advantage of these crystals is high LDT value. This is a consequence of the higher phonon energy due to the presence of a light lithium ion in the structure and the increased thermal conductivity, as well as the lower two-photon absorption of pump radiation due to the larger band gap. In this group, the highest LDT (>240 MW cm^{-2}) is shown for orthorhombic LiGaS$_2$ (LGS). This crystal is widely used for high average power frequency down conversion from the 1 μm spectral range,[6] although its nonlinear susceptibility ($d_{31} = 5.8$ pm V^{-1})[5] is significantly inferior to the parameters AgGaS$_2$, AgGaSe$_2$ and ZnGeP$_2$ ($d_{36} = 18, 32.4 \times 18$ pm V^{-1}, respectively[7]).

The main part of the work on LiGaS$_2$ is devoted to the development of methods for growing LiGaS$_2$ crystals, and the study of the effect of post-growth annealing in a controlled

Fig. 1 The image of the LiGaS$_2$ boule (a) and the LiGaS$_2$ cylinders (b) with axes along different crystallographic directions for measuring the thermal conductivity and the isotropic point.

atmosphere on optical properties, using optical spectroscopy methods and first-principles calculations of main output parameters.[8] The structure of some point defects responsible for the characteristic features in the absorption spectra was determined, the nonlinear susceptibility was estimated and phase matching conditions were calculated. As a result, the OPO and DPG modes were implemented.[5,6,9]

At the same time, it should be noted that there is no information about the temperature dependence of the LiGaS$_2$ lattice parameters and optical characteristics, as well as the thermal conductivity. Thus, for the thermal conductivity of LiGaS$_2$, only preliminary estimates based on results of the vibrational spectroscopy are known to date: 6.2 to 8.0 W $(m^{-1}\ K^{-1})$ depending on crystallographic direction.[10] The values of the heat capacity of LiGaS$_2$ in the range of 180 to 460 K are given in ref. 11.

This paper presents the results concerning temperature effects in XRD diffractograms for LiGaS$_2$, thermogravimetric analysis, differential scanning calorimetry and thermal conductivity, as well as temperature dependence of the band gap, birefringence, PL, thermo- and pyroluminescence. Such studies are important for the identification of phase transitions in LiGaS$_2$, calculations in the study of temperature fields during crystal growth and for explaining the reasons for high LDT values, as well as for determining the parameters of point

defects and evaluating the prospects for creating new optical devices based on LiGaS$_2$.

2. Results and discussion

2.1. Crystals and their structure

The grown LiGaS$_2$ single crystals were up to 20 mm in diameter and up to 50 mm long (Fig. 1a). The color of the grown boule varies from colorless to light yellow, depending on the set of defects. The transmission spectrum for a 2 mm thick LiGaS$_2$ plate measured at room temperature is shown in Fig. 2. The transparency range is 0.326–12.7 μm at room temperature.

For laser applications, colorless crystals with maximum transparency and minimal light scattering are selected. For measuring the thermal conductivity and experiments with an isotropic point, polished cylinders made of LiGaS$_2$ (Fig. 1b). LiGaS$_2$ crystals are resistant to temperature changes and can withstand temperature variations in the studied range (77–1000 K), and are suitable for use in various devices.

All peaks were indexed by orthorhombic cell ($Pna2_1$) with parameters close to LiGaS$_2$,[12] refinement was stable and gives low R-factors (Table 1 and Fig. 3). The z coordinate of Ga ion was fixed because of $Pna2_1$ space group has origin in 2_1 axis and this requires fixing z coordinate of one ion. Coordinates of atoms
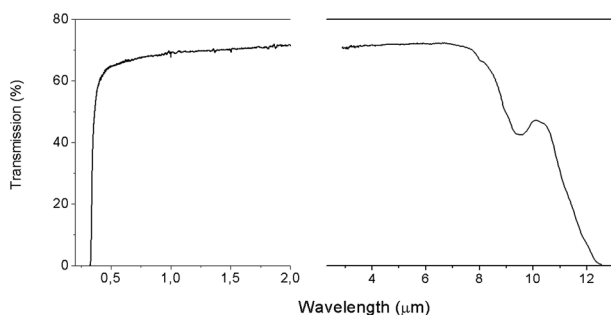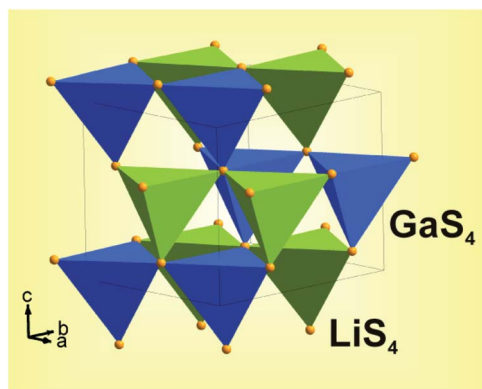

Fig. 2 Room-temperature transmission spectrum for a 2 mm thick plate cut from as grown LiGaS$_2$.

Table 1 Main parameters of processing and refinement of the LiGaS$_2$ sample

Compound	LiGaS$_2$
Space group	$Pna2_1$
a, Å	6.51625(7)
b, Å	7.86428(8)
c, Å	6.22055(6)
V, Å^3	318.776(6)
Z	4
2θ-interval, °	10–140
R_{wp}, %	6.63
R_p, %	5.21
R_{exp}, %	2.78
χ^2	2.39
R_B, %	2.27

Fig. 3   Crystal structure of LiGaS$_2$.

Fig. 4   TGA-(black line) and DSC-curves (red) for the LiGaS$_2$ crystal. The heating rate is 10 K min^{-1} in a helium atmosphere.

and main bond lengths are in Tables S1 and S2† respectively. Crystal structure is presented in Fig. 3. To get information on the temperature dependence of the unit cell parameters, 22 X-ray patterns in range 2θ-5–120° were collected from 303 K to 723 K spending 35 minutes on each pattern.

Tables with fractional atomic coordinates and isotropic displacement parameters (Table S1) and main bond lengths of LiGaS$_2$ (Table S2) are given in the ESI.†

The S-atom lattice is very nearly perfectly hexagonal closest packed. The metal atoms occupy one half of the tetrahedral interstices, namely all tetrahedra which point in the +z direction, but are ordered on these sites so that the Li and the Ga atoms populate alternate puckered (220) sheets.[12] The tetrahedra with Ga are smaller than those containing Li and mean S–S distances are 3.733 and 3.973 Å respectively. The Ga atom is displaced from the center of its tetrahedron towards the base by about 0.08 Å, giving rise to the long Ga…S bond. Similar but somewhat larger displacement takes place for Li.

The LiGaS$_2$ structure is similar to that of the enargite mineral, which is the orthorhombic form of Cu$_3$AsS$_4$, with the $Pmn2_1$ space group. The latter has closely similar cell dimensions but with interchange of the a and b dimensions. In both structures the tetrahedrally coordinated cations may be regarded as occurring in strings parallel to [010], [210] and [2ī0]. In LiGaS$_2$ each [010] string consists of alternate Li and Ga atoms; the other strings contain pairs of Li atoms alternating with pairs of Ga atoms. The puckered (220) sheets govern the registration between the strings. The present compound is strictly isostructural with LiGaO$_2$ and with β-NaFeO$_2$.[13]

2.2.   TGA and DSC results

The TGA-DSC results for LiGaS$_2$ are shown in Fig. 4. When a single-crystal LiGaS$_2$ sample is heated in a high-purity helium atmosphere (Fig. 4), an endothermic peak (onset 1224 K) is first observed on the DSC curve. At the same time, the mass of the sample is practically unchanged. The melting point of the sample is defined as 1304 $\pm$ 7 K, which is quite well consistent with the previously obtained 1298 $\pm$ 7 K data.[11] After melting, there is a noticeable loss of mass, due to the process of incongruous evaporation of the sample.[11] Features in the range of 1200–1300 K can be associated with the phase transition.
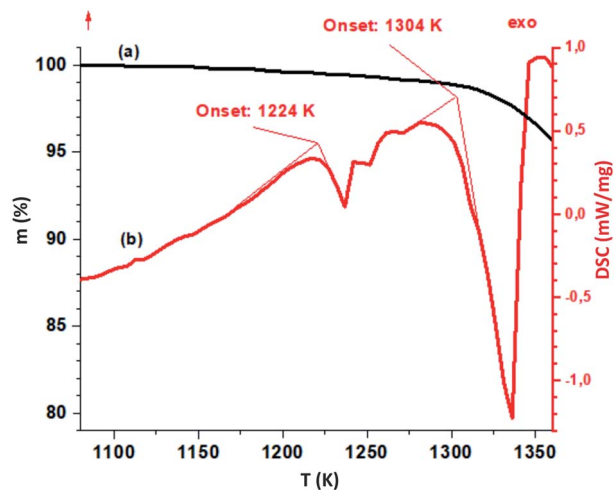
2.3.   Temperature dependences in XRD

Fig. 5 shows the temperature dependences in the range of 280–750 K for the lattice parameters a, b, c and the volume of the unit cell V in LiGaS$_2$ (blocks (a–d), respectively). It can be seen that all the lattice parameters increase monotonically with increasing temperature, as in the case of other crystals of the LiBC$_2$ family with an orthorhombic structure (LiInS$_2$, LiInSe$_2$ LiGaSe$_2$). The thermal expansion coefficients $\Delta L/(L \times \Delta T)$ for LiGaS$_2$ are $a_X = 8.13 \times 10^{-6}$, $a_Y = 18.9 \times 10^{-6}$, and $a_Z = 6.83 \times 10^{-6}$. An important advantage of such crystals in comparison with crystals with the chalcopyrite structure is a less pronounced anisotropy in the thermal expansion coefficients along different crystallographic directions. In the AgGaS$_2$, AgGaSe$_2$, and ZnGeP$_2$ crystals with the chalcopyrite structure, the thermal expansion coefficients along and across the optical axis are quite significant in magnitude, but on the other hand they have a different sign. As a result, when the temperature changes a crystal expands in one direction and contracts in the other. For example, for silver thiogallate, $\alpha\,(\perp_c) = 12.5 \times 10^{-6}$ and $\alpha\,(\|_c) = -13.2 \times 10^{-6}$, and this significantly complicates the growth of large crystals of high optical quality.

To clarify the situation with a possible phase transition near 1224 K, the XRD studies of the LiGaS$_2$ sample was performed with gradual heating until the temperature of the assumed phase transition was reached (Fig. 6). It was found that there is no phase transition, and an additional phase appears above 980 K, the amount of which increases to 1180 K and decreases above 1230 K with the restoration of the reflex intensities of the original LiGaS$_2$ phase. From Fig. 6, it can be seen that the detected compound is stable in the temperature range of 980–1230 K. A comparison of the position of the diffraction peaks (Fig. S2 in ESI†) of the detected additional phase and the LiGaO$_2$ compound suggests that the new phase is an oxygen-containing compound.[14] A slight shift of the reflexes towards lower values of 2Theta indicates an increase in the lattice parameters, which
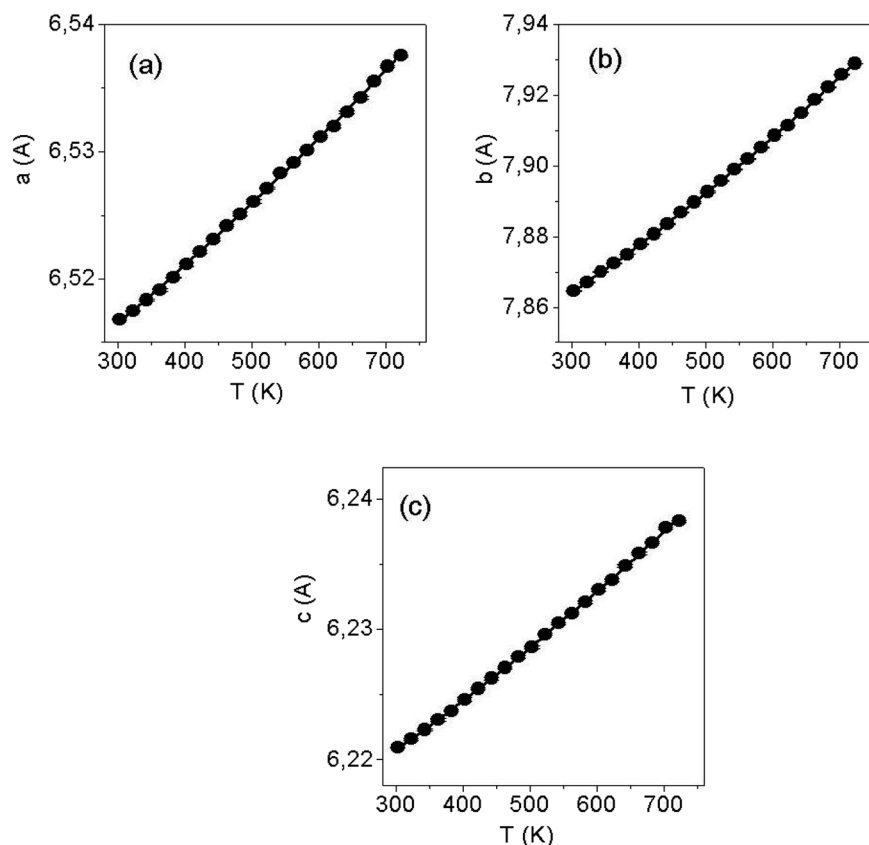
Fig. 5 Thermal dependences of cell parameters *a* (a), *b* (b) and *c* (c) of LiGaS$_2$.

may be due to partial sulfur substitution with O^{2-} anions and the formation of an isostructured LiGaO$_{2-x}$S$_x$ compound of rhombic symmetry (*Pna*2$_1$). Thus, the thermal effect detected on the DSC curve indicates the dissolution of LiGaO$_{2-x}$S$_x$ in LiGaS$_2$ in a certain temperature range.

Fig. 6 A series of X-ray diffractograms of the LiGaS$_2$ sample obtained in a high vacuum (~5 × 10^{-4} mBar) at temperatures in the range of 780–1230 K. The dotted line shows the most intense reflexes related to the oxygen-containing phase. On the diffractogram obtained at *T* = 1080 K, all reflexes related to this phase, supposedly LiGaO$_{2-x}$S$_x$, are marked with asterisks.

2.4. Thermal diffusivity and thermal conductivity in LiGaS$_2$

To measure the thermal conductivity, one of the non-stationary methods was used, in which the thermal diffusivity is directly measured, and then calculated taking into account the known values of the heat capacity and density. The thermal diffusivity δ is a physical quantity that characterizes the rate of change (equalization) of the temperature of a substance in nonequilibrium thermal processes. Numerically, the thermal conductivity is equal to the ratio of the thermal conductivity to the specific heat capacity at constant pressure c_p. The thermal conductivity of the crystal χ can be calculated using the following formula:[15]

$$\chi = \delta \times c_p \times \rho, \qquad (1)$$

where ρ is density.

Measurements at a given temperature T were carried out in a series of two "flashes" of the laser after the sample was thermostated. The interval between the "flashes" was 3 minutes. Since LiGaS$_2$ is transparent at the wavelength of the laser light source generation, the samples were previously coated with a layer of graphite on both ends to increase the absorption capacity of the surfaces. The measurement error of α for solid samples on the LFA-427 unit is 2–5%, depending on the temperature. The obtained values of thermal diffusivity for LiGaS$_2$ and the values of thermal conductivity calculated from
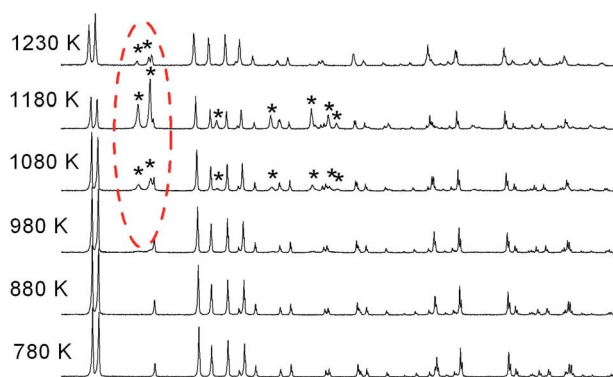
Table 2 Coefficients of thermal diffusivity δ and thermal conductivity χ for LiGaS$_2$, LiInS$_2$ and AgGaS$_2$

Crystallographic direction, mode	T, K	δ for LiGaS$_2$, mm^2 s^{-1}	χ for LiGaS$_2$ W (m^{-1} K^{-1})	χ for LiInS$_2$, W (m^{-1} K^{-1})	χ, for AgGaS$_2$, W (m^{-1} K^{-1})
X	296.5	4.662	8.440	6.2 (ref. 16)	1.5 (ref. 16)
Y, heating	296.7	5.031	9.108	6.0 (ref. 16)	1.5 (ref. 16)
	371.7	3.725	7.141		
	470.7	2.635	5.222		
	571.9	2.061	4.267		
Y, cooling	573.6	2.035	4.213		
	473.3	2.659	5.345		
Z	296.6	5.556	10.058	7.6 (ref. 16)	1.4 (ref. 16)

them according to the formula (1) for various crystallographic directions (X, Y, Z), as well as the temperature dependence in the range of 20–300 °C for χ_Z, are presented in Table 2 and Fig. 7. The calculations used the values of the specific heat capacity c_p at 300 and 460 K for LiGaS$_2$: 90.08 and 98.6 J mol^{-1} K^{-1}, respectively, as well as molecular mass $M = 140.78$ g mol^{-1} (ref. 17) and density (specific gravity) 2.94 g cm^{-3}.[1] The thermal expansion of the samples was not taken into account. Previously, based on the data of vibrational spectroscopy, the values of thermal conductivity at 300 K for LiGaS$_2$ were estimated in the range of $6 \div 8$ W (m^{-1} K^{-1}).[16] The values of the thermal conductivity χ, measured by us experimentally, were even about 25% higher: 8.440, 9.108 and 10.058 W mK^{-1} along X, Y, Z, respectively. The maximum values of χ are obtained for room temperature along Z direction. In Fig. 7a one can see that with an increase in temperature to 580 K, the thermal conductivity decreases by more than 2 times. Also for this sample, the thermal conductivity during cooling in the region of 473 K was measured and a good agreement with the data obtained during heating was established. Such behavior of thermal conductivity as a function of temperature is characteristic of the dominant lattice (phonon) contribution to the total thermal conductivity.

Fig. 7b compares the thermal conductivity values for commercial AgGaS$_2$ and AgGaSe$_2$, and the values for members

of the LiBC$_2$ family, for which the thermal conductivity has so far been measured experimentally. As you know, the thermal conductivity of materials or energy transfer is determined by elastic vibrations (phonons), and above all by their energy. In turn, the latter is determined by the mass of the participating ions and the energy of the phonons increases with decreasing ion mass. As a consequence, the thermal conductivity is relatively low in silver thiogallate and, as our experiments show, it is almost 7 times higher in lithium thiogallate. Thus, LiGaS$_2$ effectively implements energy dissipation under local heating in the laser scheme and the crystal has a high optical damage threshold. The literature provides LDT values of 34, 40, and more than 240 MW cm^{-2} at pumping with 1.064 nm, 15 ns pulses for AgGaS$_2$, LiInS$_2$, and LiGaS$_2$, respectively.[16]

2.5. Thermooptic effects in LiGaS$_2$

2.5.1. Birefringence. Studies were carried out to determine the nature of the anomaly in DSC at $T \sim 1223$ K. The reason for this anomaly may be a phase transition with a decrease in symmetry, for example, from rhombic polar symmetry to rhombic centrosymmetric: $mm2 \leftrightarrow mmm$. In this case, at room temperature, there would have to be twins with a multidirectional polarization of $\pm P$, which can be detected by etching
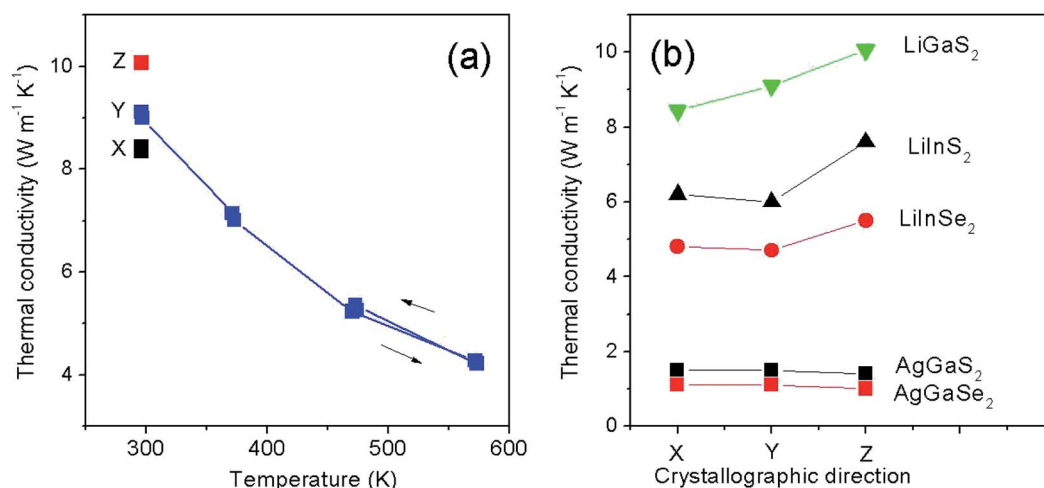

Fig. 7 Thermal conductivity for chalcogenides: (a) LiGaS$_2$ along X, Y and Z directions at room temperature and temperature deendence for χ_Z in the 300 to 557 K range. Arrows indicate heating or cooling regime. (b) Comparison of values for commercial AgGaS$_2$, AgGaSe$_2$ and for crystals of the LiBC$_2$ family with B = In, Ga and C=S, Se.
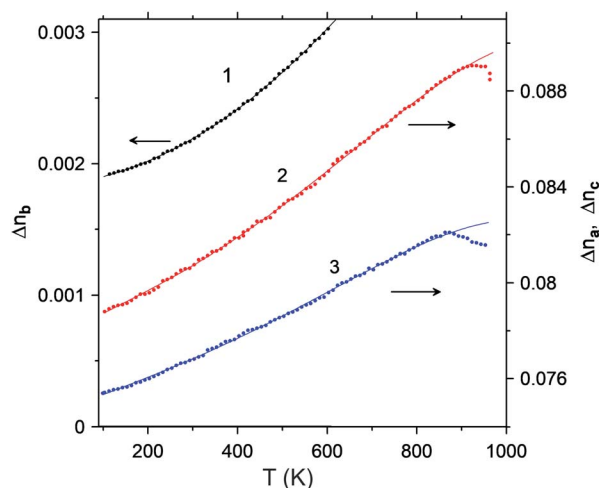
Fig. 8   Temperature dependences of the birefringence of LiGaS$_2$ at a wavelength of about 400 nm: (1) Δn_b, (2) Δn_c, (3) Δn_a.

Fig. 10   Transmission spectra for (100) LiGaS$_2$ plate with a thickness of 5 mm placed between crossed (1) and parallel (2) film polarizers.

(001) LiGaS$_2$ plates. Specially conducted experiments on etching in dilute bechromate at room temperature showed only etching of scratches, while domains or twins were not detected.

Fig. 8 shows the temperature dependence of the birefringence measured in a wide range from 373 K to 1173 K. Features at temperatures above 870 K are associated with the degradation of the polished surface of the crystals: at a higher temperature, the surface becomes matte. The crystal is vaporized, as a result of which the upper surface is covered with plaque flakes, while the lower surface remains unchanged. It can be seen that the birefringence measured at 400 nm increases monotonically and approximately linearly with an increase in temperature from 100 to 950 K. Curves 1–3 are smooth and no special features are detected: thus, there are no phase transitions in this range.

Fig. 9 shows the birefringence dependence of Δn_b, Δn_c and Δn_a. for a biaxial LiGaS$_2$ crystal from the wavelength in the range of its transparency. It can be seen that the birefringence values Δn_a and Δn_c are quite close to each other (~0.04), but they are both quite far from Δn_b. In this case, the dependence

$\Delta n_b = f(T)$ passes through zero twice, *i.e.* there are two so-called isotropic points. Fig. 10 shows the transmission spectra for a LiGaS$_2$ plate located between two polaroids when they are crossed (curve (1)) and when the polaroids are parallel (2). In this case, the spectra show characteristic anomalies in the visible region of the spectrum in the form of a narrow dip (1) and in the form of a narrow passband (2) at the same wavelength. A similar feature was previously observed in some anisotropic crystals in the presence of natural or induced gyrotropy at the wavelength of the isotropic point. Examples of such crystals are double single crystals of CdS, CdSe, ZnO, AgJ, MnF$_2$, Al$_2$O$_3$, ZnTe, and mixed compounds based on these crystals.[18] Of the triple chalcogenides used in nonlinear optics, such narrow-band filtration was previously observed in AgGaS$_2$ and AgGaSe$_2$ crystals with a chalcopyrite structure (symmetry-$42m$).[19]

At room temperature, for the (100) LiGaS$_2$ plate, both features are located at 451.5 nm, and they correspond to one of the isotropic points. Another similar feature is expected in the mid-IR, at about 7 μm. It is established that the position of the described line significantly depends on the temperature. Fig. 11 shows a set of transmission lines for the case of crossed
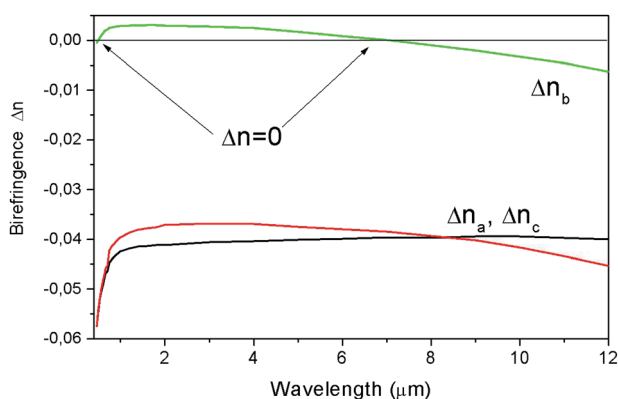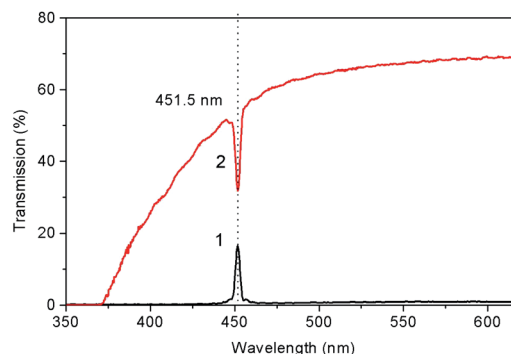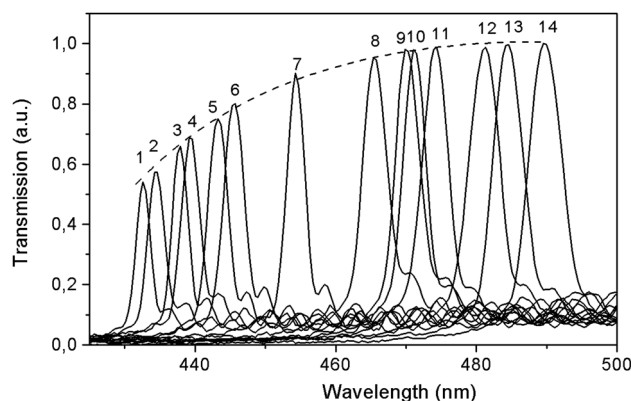

Fig. 9   Dependence of the birefringence Δn on the wavelength for LiGaS$_2$. The arrows show two isotropic points, where $\Delta n = 0$.

Fig. 11   Transmission spectra for a (100) LiGaS$_2$ plate 5 mm thick placed between the crossed polarizers. Spectra were measured at fourteen different temperatures in the temperature range of 77 K (curve (1)) to 550 K (14).
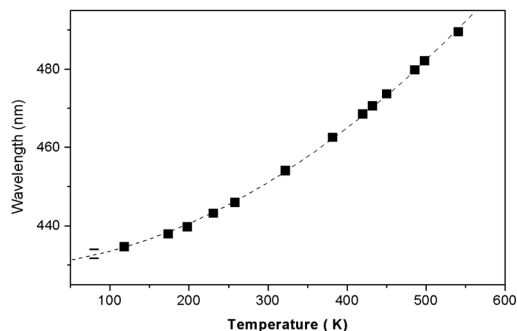
Fig. 12 The position of the isotropic point as a function of temperature. The dependence is approximated by the polynomial $Y = A + B_1^* X + B_2^* X^2$, where the parameter values are $A = 429.75$, $B_1 = 0.02$, and $B_2 = 1.7 \times 10^{-4}$.

Fig. 14 PL spectra recorded at $T = 80$ K, at 300 nm (1) and 375 nm (2) excitation for LiGaS$_2$ annealed in vacuum. The insert shows the room temperature PL patterns obtained at UV excitation with 300 nm light (upper image with orange emission) and 375 nm (lower image with blue PL).

polarizers, when the temperature of the LiGaS$_2$ crystal varied in the range from 77 to 550 K (points 1–14). At the same time, the position of the line is shifted from 430 to 490 nm, respectively.

Fig. 12 shows the dependence of the position of the isotropic point in the visible region of the spectrum as a function of temperature. This dependence is well approximated by the dependence $Y = A + B_1^* X + B_2^* X^2$, where the parameter values are $A = 429.75$, $B_1 = 0.02$, and $B_2 = 1.7 \times 10^{-4}$. The value of the line width at half-height gradually changes from 2.4 at 77 K to 5.4 nm at 550 K with a spectral resolution of about 0.5 nm. Thus, the LiGaS$_2$ plate in combination with two polarizers can be used as a narrow-band optical filter, smoothly tunable by changing the temperature of the crystal (Fig. 13).

2.5.2. Temperature dependence of the band gap. The fundamental absorption edge for LiGaS$_2$ is at about 326 nm in the UV region. The Tauc analysis of the shape edge shows the straightening in the coordinates $(k \times h\nu)^2 = f(h\nu)$, where k is the absorption coefficient, and $h\nu$ is the photon energy.[20] This
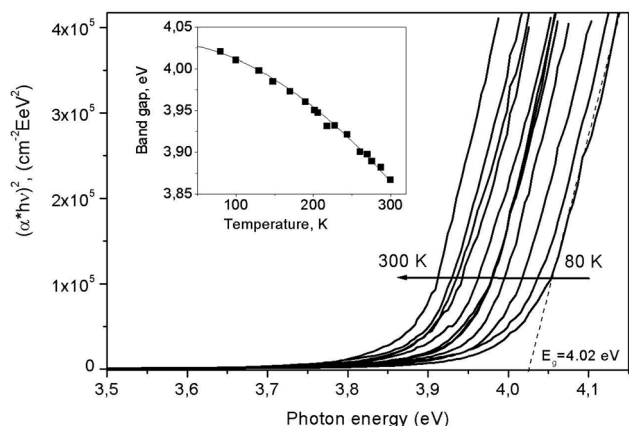

Fig. 13 Absorption spectra for LiGaS$_2$ in the region of the fundamental absorption edge, measured at 12 different temperatures in the range from 77 to 300 K and presented in coordinates $(\alpha h\nu)^2 = f(h\nu)$ (Tauc plot). The insert shows the temperature dependence for the band gap in LiGaS$_2$. The points are obtained experimentally, while the line shows the result of the approximation in accordance with the Varshni equation.[21]
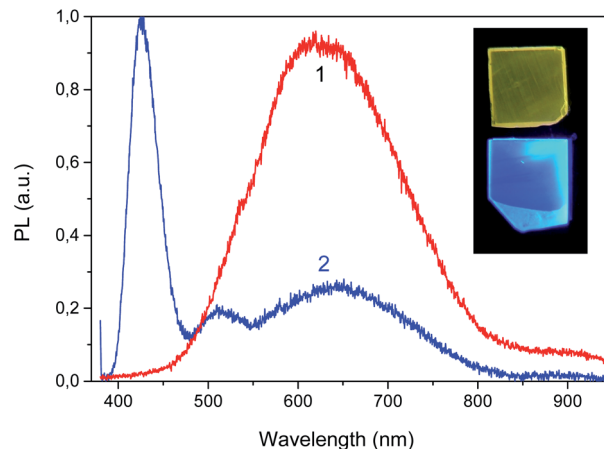
indicates that for LiGaS$_2$, direct allowed electronic transitions are responsible for band-to-band electronic transitions. LiGaS$_2$ crystals have a band gap E_g of 3.88 eV at room temperature, which is the maximum value among ternary chalcogenides. For AgGaS$_2$ and LiInS$_2$, the E_g values are 2.7 and 3.57 eV, for selenides these values are even lower.[16] As a result, LiGaS$_2$ crystals are almost colorless compared to the substantially colored crystals of other ternary chalcogenides. As a result, at 800 nm excitation LiGaS$_2$ is characterized by a two-photon absorption coefficient (TPA) of about 0.01 cm GW^{-1}, which is significantly lower than the values for AgGaS$_2$ (3.5 cm GW^{-1}) and LiInS$_2$ (0.04 cm GW^{-1}).[16] This reduces the energy absorbed during pumping and reduces the danger of crystal optical damage when using it in OPO.

Fig. 14 shows such constructions for 12 different temperatures in the range of 77–300 K. It can be seen that the absorption edge shifts towards lower energies as the temperature increases. In this case, the band gap E_g, determined by the intersection of the approximating line with the abcissa axis, increases from 4.03 eV at 77 K to 3.88 eV at 300 K. The insert in Fig. 14 shows the temperature dependence for E_g. We found that it is well described by the semi-empirical Varshni equation:[21]

$$E_g(T) = E_0 - \alpha_1 T^2/(T + \beta_1) \qquad (2)$$

where E_0 is the band gap at $T = 0$, while the parameters $\alpha_1 = 4 \times 10^{-3}$ and $\beta_1 = 1850$ K.

2.5.3. Temperature dependence of photoluminescence (PL). The PL spectra for LGS as-grown and after annealing in different atmospheres have been studied in detail in our works.[8] The following main features have been identified in the PL spectra: (1) two bands of about 416 and 452 nm responsible for sulfur vacancies in crystallographically different positions in the LGS lattice (F-centers), both types of PL being excited in the same band of 375 nm near the edge of fundamental absorption; and (2) a wide band with a maximum in the range of 550–
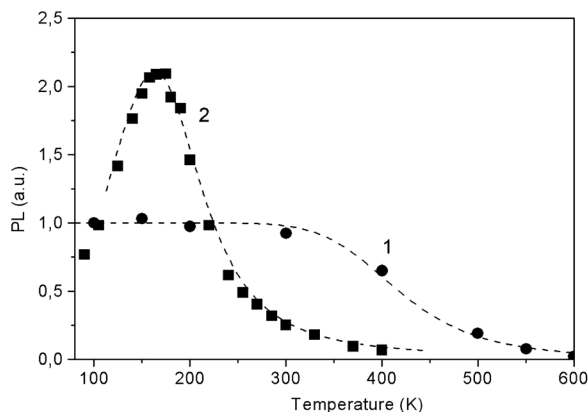
Fig. 15 The temperature dependence of the integral PL in the bands of about 600 nm (1) and 425 nm (2) in LiGaS$_2$ at excitation of 300 and 375 nm, respectively. The dots represent the experimental data, while the dotted curves show the results of calculations according to eqn (3) with the parameters $\Delta E = 0.14$ eV, $\tau_R \nu_0 = 4 \times 10^3$ (1) and $\Delta E = 0.35$ eV, $\tau_R \nu_0 = 1.7 \times 10^4$ (2).

620 nm excited most efficiently during band-to-band electronic transitions and associated with self-trapped excitons (STE) at different point defects.[22] The blue PL in the 425 nm band is characteristic of LiGaS$_2$ crystals with anion deficiency, which occurs, for example, after sample annealing in vacuum.

The temperature dependence for the PL glow in the main bands is shown in Fig. 15. For both PL bands temperature dependence is well described by the Mott model for two recombination channels, one radiative and one non-radiative, from the relaxed excited state.[23] Here the temperature dependence of quantum efficiency η follows the expression:

$$\eta(T) \approx 1/(1 + \tau_R \nu_0 \exp(-\Delta E/kT)) \qquad (3)$$

where τ_R is the radiative lifetime at low temperature, ΔE is the energy barrier to the nonradiative decay route, and ν_0 is a jump frequency. The proportional sign is used because other non-radiative decay channels must be available before the system reaches the relaxed excited state.

Fig. 15 shows the experimental points and the results of their approximation for the orange and blue glow (dotted curves). For the blue glow of V_S, the parameters $\Delta E = 0.35$ eV and pre-exponential factor $\tau_R \nu_0 = 1.7 \times 10^4$ are well suited, while for the orange glow of STE, the parameters are $\Delta E = 0.14$ eV and $\tau_R \nu_0 = 4 \times 10^3$. In the case of STE, there is an initial stage of PL rise with an activation energy of $\Delta E_1 \sim 0.02$ eV, which indicates the need to overcome a small activation barrier for exciton self-localization. Thus, in the case of LiGaS$_2$, it is possible to directly cause intense blue room-temperature PL by special post-growth annealing crystal in vacuum. At 365 nm excitation, the quantum yield of PL in LGS is estimated relative to Rhodamine 640 with a quantum yield η close to unity. At room temperature, the values of η are about 0.1 for the blue luminescence of F-centers and 0.0095 for the glow of STE. As can be seen from Fig. 15, the intensity of blue PL flares increases about 10 times when the temperature drops to 180 K, whereas with

a further decrease in temperature, some weakening of the PL is observed. A completely different behavior is demonstrated by a weaker exciton PL: it is constant in the low-temperature range and quenched above room temperature. Low values of η make it difficult to widely use LGS at room temperature, but at 180 K the quantum yield of the blue PL is close to unity. Nevertheless, the analysis of the PL spectra allows us to obtain valuable information about the conditions for growth or annealing crystals, as well as about the state of point defects. It should be noted that a similar (in the blue region) PL associated with F-centers is also observed in LiInS$_2$.

To date, this is the only known case of bright photoluminescence at room temperature in the visible region of the spectrum among the crystals of ternary chalcogenides, including the LiBC$_2$ family. The crystal is considered as promising for use in various optical devices including active media for lasers and light sources.

2.5.4. Thermoluminescence (TL). The analysis of TL curves provides valuable information about the parameters of shallow levels in the band gap.[24] The UV illumination of LiGaS$_2$ crystals at low temperature is accompanied by the accumulation of a significant light sum. The TL curve obtained by further heating the crystal in the dark is shown in Fig. 16. The analysis of the peaks shape shows that they are rather symmetric and the values of full width at half-maximum (FWHM) at rise and at decay are rather close. This indicates a second order of TL kinetics when the probability of recombination of free carriers is negligible compared with the probability of their retrapping.[24]

The shape of TL peak is described by the following expression:[24]

$$I(T) = n_0^2 \, s \, \exp\left(-\frac{E_T}{kT}\right) \bigg/ \left[1 + (n_0 s/\beta) \times \int_{T_0}^{T} \exp\left(-\frac{E_T}{kT}\right) dT\right]^2 \qquad (4)$$

where n_0 is the initial concentration of electrons, s is the escape factor, β is the rate of linear heating (K min^{-1}), k is the Boltzmann's constant, E_T is the thermal activation energy (eV) and T_0
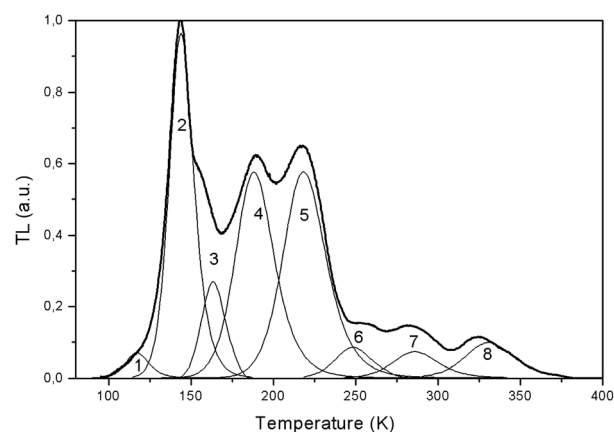

Fig. 16 TL curve for LiGaS$_2$ after 365 nm excitation at 80 K and the results of deconvolution into 8 components (shown in thin lines). The resulting parameters for the corresponding capture centers are shown in the Table 3 below.

Table 3 Parameters of traps in LiGaS$_2$ (results of decomposition)

NN	Peak maximum position, K	Thermal activation energy, eV	Preexponential coefficient, s^{-1}
1	115	0.23	10^8
2	144	0.31	3×10^{10}
3	156	0.45	3×10^{12}
4	190	0.36	10^8
5	217	0.44	3×10^8
6	256	0.67	10^{12}
7	283	0.72	10^{11}
8	324	0.90	10^{12}

is the initial temperature. Position of eight TL maxima as well as the results of calculations (parameters E_T and s) are given in Table 3. There is a good coincidence between the sum of these components and the experimental curve (curve shown in bold black).

It can be seen that the TL glow is localized mainly in the low-temperature region of 140–240 K: exactly where the peak in the temperature dependence of the STE luminescence is observed (Fig. 15). It is possible that the traps are involved in the process of radiative recombination of STE maybe as a result of intermediate localization of charge carriers on traps.

2.5.5. Pyroelectric luminescence (PEL) of LiGaS$_2$. When LiGaS$_2$ crystals are heated or cooled in the dark, without any excitation, a spontaneous glow is observed in the form of a sequence of short pulses (flashes) in the temperature range of 80–350 K. In Fig. 17 the emission intensity in LiGaS$_2$ is shown as a function of the temperature in the cooling (a) and heating (b)
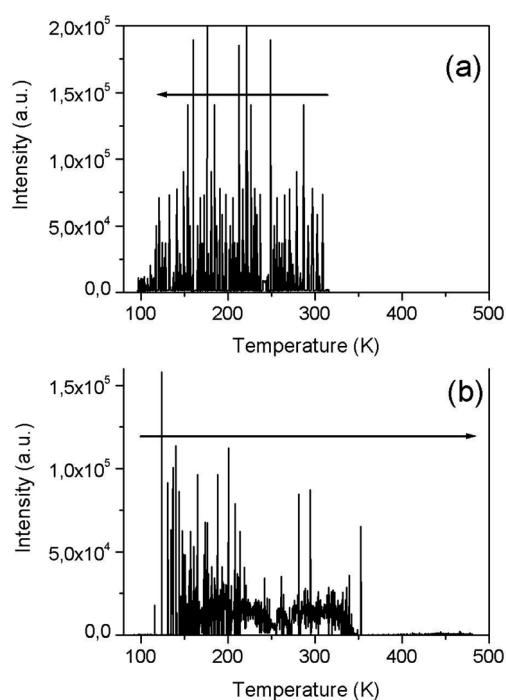

Fig. 17 Temperature dependence of spontaneous luminescence in LiGaS$_2$ in the cooling (a) and heating (b) modes.

modes. Such a glow in the dark, without any special excitation, is characteristic only of pyroelectrics and is the result of a restructuring in the atomic polarization in the crystal at a temperature change.[25] This is in good agreement with the results of structural studies in ref.,[12] where the XRD study determined the symmetry of the LiGaS$_2$ as mm^2 space group of the monoclinic system (without a center of symmetry). Spontaneous light flashes are a result of the dielectric break-down and they happen on both crystal surface and inside it. We have observed the PEL effect in many typical nonlinear optical crystals such as LiIO$_3$, β-BaB$_2$O$_4$ (BBO), LiB$_3$O$_5$ (LBO), Ag$_3$AsS$_3$, LiNbO$_3$, LiGaS$_2$, KTP, LiGaSe$_2$, and LiGaGe$_2$Se$_6$ (LGGSe).[25] On the other hand, the PEL is absent in AgGaS$_2$ and AgGaSe$_2$ with a chalcopyrite structure (space group $I\bar{4}2d$) which are not pyroelectrics. The absence of PEL at temperature greater than 440 K is the result of an increase in electrical conductivity as temperature grows. This increase in conductivity promotes the leak of the pyroelectric charge and the break-down probability becomes smaller. The PEL effect indicates a relatively low LiGaS$_2$ conductivity and, in turn, a low concentration of electrically active defects. PEL intensity decreases until it completely disappears when the crystals are illuminated or after their preliminary illumination: this is due to an increase in electrical conductivity as a result of such processing and charge runoff. It is assumed that PEL can also occur as a result of local heating of a nonlinear crystal during operation in a laser scheme and be one of the mechanisms of laser damage to crystals.

3. Conclusions

(1) Large LiGaS$_2$ crystals with a length of up to 50 mm, a diameter of up to 20 mm, of high optical quality were grown.

(2) DSC shows anomalies of about 1224 K, at a temperature below the melting point (1304 K ± 5). In this case, the lattice parameters and birefringence increase smoothly and monotonically with increasing temperature, which indicates the absence of phase transitions in LiGaS$_2$. Anomalies around 1224 K are associated with the appearance of inclusions of the type LiGaO$_{2-x}$S$_x$.

(3) The thermal conductivity χ was measured for LiGaS$_2$: the values of 8.44 (X), 9.11 (Y), and 10.05 (Z) W (m^{-1} K^{-1}) obtained at 300 K are the highest among the crystals of the LiBC$_2$ family where B = In, Ga, C = S, Se, Te. The thermal conductivity decreases with increasing temperature in the range of 300–600 K in accordance with the model of the dominant lattice mechanism.

(4) The isotropic points in the dispersion characteristics $n = f(\lambda)$ for LiGaS$_2$ are revealed. The possibility of using the crystal in narrow-band optical filters smoothly tunable by changing crystal temperature is demonstrated. The position of the transmission line changes from 430 to 490 nm when heated from 77 to 550 K, while the FWHM values increase from 2.4 to 5.4 K. Calibration curves are proposed.

(5) The Tauc analysis shows that band-to-band transitions are determined by direct allowed electronic transitions. The band

gap E_g is 4.02 and 3.93 eV at 80 and 300 K, and the dependence $E_g = f(T)$ is described by the semi-empirical Varshni law.

(6) In the PL spectra for $LiGaS_2$, the most common is the low-temperature glow of self-trapped excitons. Post-growth annealing in vacuum produces anionic V_S vacancies and corresponding intense blue PL at room temperature.

(7) The thermoluminescence curves are analyzed, and the parameters of the charge carrier capture centers with energies in the range of 0.2–0.9 eV are estimated.

(8) $LiGaS_2$ crystals exhibit pyroluminescene in the range of 80–350 K. This is consistent with the established XRD symmetry of mm^2. The latter belongs to one of the 10 crystallographic groups with a non-zero vector of spontaneous polarization.

4. Experimental section

4.1. Crystal growth

$LiGaS_2$ single crystals were grown by the Bridgman–Stockbarger method in a two-zone vertical furnace. The upper and lower parts of the furnace were separated by a diaphragm made of thermal insulation material. The temperature in the melt with an accuracy of ± 0.1 °C was maintained at 1423 K, which is ~100 K higher than the melting point of $LiGaS_2$. The axial temperature gradient was about ~2° mm^{-1}. The rate of the ampoule lowering varied in the range of 2–10 mm per day. Ga and S of 99.999% purity and Li of 99.9% purity were used as initial chemical reagents for crystal growth. The charge was poured into an ampoule made of glass graphite, which, in turn, was sealed in a quartz ampoule. This design made it possible to avoid chemical interaction between the Li and the walls of the quartz container.

4.2. X-ray diffraction studies

Powder X-ray diffraction data were collected on a PANalytical X'Pert PRO diffractometer with a solid state detector PIXcel using Cu Kα radiation over the 2θ range 15–105°. An Anton Paar HTK 1200N camera was used for the high-temperature measurements. The powder diffraction data of LiGaS2 for Rietveld analysis was collected at room temperature with a Bruker D8 ADVANCE powder diffractometer (Cu-Kα radiation) and linear VANTEC detector. The step size of 2θ was 0.016°, and the counting time was 1.5 s per step. The 2θ range of 10–70° was measured with 0.6 mm divergence slit, but 2θ range of 70–140° was measured with 2 mm divergence slit. Rietveld refinement was performed by using TOPAS 4.2 (ref. 26) which accounts esd's of each point by special weight scheme.

Larger slits allow noticeably increase intensity of high-angle peaks without loss of resolution because the high-angle peaks are broad enough to be not affected by bigger divergence beam. The esd's $\sigma(I_i)$ of all points on patterns were calculated using intensities I_i: $\sigma(I_i) = I_i^{1/2}$. The intensities and obtained esd's were further normalized: $I_{i\ norm} = I_i \times 0.6/(\text{slit width})$, $\sigma_{norm}(I_i) = \sigma(I_i) \times 0.6/(\text{slit width})$, taking into account actual value of divergence slit width which was used to measure each particular intensity I_i, and saved in xye-type file. So transformed powder pattern has usual view in whole 2θ range 10–140°, but all high-angle points have small esd's. Difference Rietveld plot of $LiGaS_2$ is given in Fig. S1 in ESI.†

4.3. Optical properties

Absorption spectra for $LiGaS_2$ were measured using a UV-2501PC Shimadzu spectrometer in the UV to near IR region and a Fourier transform spectrometer Infralum FT-801, in the mid IR. Transmission spectra at different temperatures and temperature dependences in the heating or cooling mode were measured using a metal vacuum cryostat with fused quartz windows. The transmission spectrum for a 2 mm thick $LiGaS_2$ plate measured at room temperature is shown in Fig. 3. The transparency range is 0.326–12.7 μm. Transmission spectra were obtained at 14 different temperatures in the range of 80–350 K, and in each case, the shape of the fundamental absorption edge was analyzed following Tauc[20] to determine the mechanism of band-to-band electronic transitions. In the study of pyroluminescence (PEL) and thermoluminescence (TL), the rate of change in temperature β in the range of 80–600 K during heating or cooling was maintained at 30° min^{-1} and was regulated using liquid nitrogen and an ohmic heater controlled from a temperature controller. The isotropic point was detected by characteristic narrow dips/peaks in the transmission spectra when registering the spectral dependence of the transmission of the $LiGaS_2$ sample located between two parallel-tuned or crossed film polaroids, respectively.

The photoluminescence (PL) spectra were recorded on diffraction luminescence spectrometer SDL1 with excitation from a 1 kW Xe lamp through a diffraction MDR2 monochromator. A cooled FEU83 photomultiplier sensitive up to 1.2 μm (1.03 eV) was used to detect the PL emission. The thermoluminescence (TL) curves were obtained by recording the glow of the crystal during its heating at a constant rate of 30 deg. per min after irradiation at a temperature of 80 K.

The birefringence measurements were carried out in the temperature range of 90–950 K with the use of an Axioskop-40 polarization microscope and Linkam LTS 350 and TS1500 heating stages. Birefringence was measured to an accuracy of ± 0.00001 by the Berek compensator method with the use of a Leica instrument.

4.4. Thermophysical measurements

4.4.1. TGA-DSC measurements. The simultaneous thermogravimetric analysis and differential scanning calorimetry (TGA-DSC) measurements wereas carried out with a STA 449 F1 Jupiter thermal analyser (NETZSCH, Germany). The measurements were made in a helium flow (He 99.995%) in the temperature range of 1000–1400 K using the heating rate of 10 K min^{-1}, the gas flow rate of 30 mL min^{-1} and closed Pt crucibles. The treatment of experiment results was performed using standard Proteus Analysis software.[27]

4.4.2. Thermal diffusivity and thermal conductivity. The thermal diffusivity δ of the studied samples was determined by the laser flash method on a LFA-427 installation from NETZSCH Co, Germany at room temperature in air and in an atmosphere of high-purity argon (Ar 99.992 vol%) in the temperature range of 300–580 K. The essence of this method is that a flat sample is irradiated from

below with a short 1.064 μm laser pulse[28] The IR detector registers the temperature change of the upper surface of the sample. The value of δ is determined from the obtained thermogram, taking into account the heat losses according to the model.[29] An adjustment is made for the finite duration of the laser pulse and its actual shape.[30]

Conflicts of interest

There are no conflicts to declare.

Acknowledgements

References

1 D. Nikogosyan, *Nonlinear Optical Crystals: A Complete Survey*, Springer Science + Business Media, Inc., N.-Y, 2005.

2 L. Isaenko, A. Yelisseyev, S. Lobanov, A. Titov, V. Petrov, J.-J. Zondy, P. Krinitsin, A. Merkulov, V. Vedenyapin and J. Smirnova, *Cryst. Res. Technol.*, 2003, **38**, 379.

3 H.-M. Zhou, L. Xiong, L. Chen and L.-M. Wu, *Angew. Chem., Int. Ed.*, 2019, **58**, 9979.

4 L. Isaenko, I. Vasilyeva, A. Merkulov, A. Yelisseyev and S. Lobanov, *J. Cryst. Growth*, 2005, **275**, 217.

5 V. Petrov, A. Yelisseyev, L. Isaenko, S. Lobanov, A. Titov and J.-J. Zondy, *Appl. Phys. B*, 2004, **78**, 543.

6 (*a*) A. Tyazhev, V. Vedenyapin, G. Marchev, A. Yelisseyev, L. Isaenko, D. Kolker, M. Starikova, S. Lobanov, V. Petrov and J.-J. Zondy, *Opt. Mater.*, 2013, **35**, 1612; (*b*) S. N. Smetanin, M. Jelínek, V. Kubeček, A. F. Kurus and L. I. Isaenko, *2018 Conf. on Lasers and Electro-Optics Pacific Rim, CLEO-PR*, 2018–2019.

7 (*a*) G. Boyd, H. Kasper and J. McFee, *IEEE J. Quantum Electron.*, 1971, **7**, 563; (*b*) H. Kildal and J. C. Mikkelsen, *Opt. Commun.*, 1973, **9**, 315; (*c*) G. D. Boyd, E. Buehler and F. G. Storz, *Appl. Phys. Lett.*, 1971, **18**, 301.

8 (*a*) A. Yelisseyev, Z. S. Lin, M. Starikova, L. Isaenko and S. Lobanov, *J. Appl. Phys.*, 2012, **111**, 113507; (*b*) A. P. Yelisseyev, M. K. Starikova, V. V. Korolev and L. I. Isaenko, *J. Opt. Soc. Am. B*, 2012, **29**, 1003.

9 (*a*) V. Vedenyapin, A. Boyko, D. Kolker, L. Isaenko, S. Lobanov, N. Kostyukova, A. Yelisseyev and V. Petrov, *Laser Phys. Lett.*, 2016, **13**, 115401; (*b*) S. Qu, H. Liang,

10 L. Isaenko, A. Yelisseyev, S. Lobanov, P. Krinitsin, V. Petrov and J.-J. Zondy, *J. Non-Cryst. Solids*, 2006, **352**, 2434.

11 V. Drebushchak, L. Isaenko, S. Lobanov, P. Krinitsin and S. Grazhdannikov, *J. Therm. Anal. Calorim.*, 2017, **129**, 103.

12 J. Leal-Gonzalez, S. S. Melibary and A. J. Smith, *Acta Crystallogr., Sect. C: Struct. Chem.*, 1990, **46**, 2017.

13 M. Marezio, *Acta Crystallogr.*, 1965, **18**, 481.

14 G. M. Kuz'micheva, V. B. Rybakov, A. V. Gaister and E. V. Zharikov, *Inorg. Mater.*, 2001, **37**, 281–285.

15 R. Berman, *Thermal conduction in solids*, Clarendon Press, 1976.

16 (*a*) L. Isaenko, A. Yelisseyev, S. Lobanov, P. Krinitsin, V. Petrov and J.-J. Zondy, *J. Non-Cryst. Solids*, 2006, **352**, 2434; (*b*) L. Isaenko and A. Yelisseyev, *Semicond. Sci. Technol.*, 2016, **31**, 123001.

17 Q. Li, J. Wei, H. Sun, K. Zhang, Z. Huang and L. Zhang, *Sci. Rep.*, 2017, 7, 13747.

18 (*a*) G. H. Henry, *Phys. Rev.*, 1966, **143**, 627; (*b*) R. B. Parson, W. Wardzynski and A. D. Yoffe, *Proc. R. Soc. London, Ser. A*, 1961, **262**, 120; (*c*) J. J. Hopfield and D. C. Thomas, *Phys. Rev. Lett.*, 1965, **15**, 22.

19 (*a*) M. V. Hobden, *Acta Crystallogr., Sect. A: Cryst. Phys., Diffr., Theor. Gen. Crystallogr.*, 1968, **24**, 676; (*b*) M. V. Hobden, *Acta Crystallogr., Sect. A: Cryst. Phys., Diffr., Theor. Gen. Crystallogr.*, 1969, **25**, 633.

20 J. Tauc, *Mater. Res. Bull.*, 1967, **3**, 37.

21 Y. P. Varshni, *Physica*, 1967, **34**, 149.

22 K. S. Song and R. T. Williams, *Self-trapped excitons*, Springer, 1993.

23 B. Henderson and G. F. Imbusch, *Optical Spectroscopy of Inorganic Solids*, Clarendon, 1989.

24 S. W. S. Mc Keever, *Thermoluminescence of solids*, Cambridge Uni. Press, Cambridge, London, New-York, 1988.

25 (*a*) A. P. Yelisseyev, L. I. Isaenko and M. K. Starikova, *J. Opt. Soc. Am. B*, 2012, **29**, 1430; (*b*) A. Yelisseyev, F. Liang, L. Isaenko, S. Lobanov, A. Goloshumova and Z. S. Lin, *Opt. Mater.*, 2017, **72**, 795; (*c*) A. Yelisseyev, L. Isaenko, P. Krinitsin, F. Liang, D. Naumov, A. Goloshumova and Z. S. Lin, *Inorg. Chem.*, 2016, **55**, 8672.

26 *Bruker AXS TOPAS V4: User's Manual*, Bruker AXS, Karlsruhe, Germany, 2008.

27 *NETZSCH Proteus Thermal Analysis v.6.1.0 – NETZSCH-Gerätebau GmbH – Selb/Bayern*, Germany, 2013.

28 (*a*) W. J. Parker, R. J. Jenkins, C. P. Butler and G. L. Abbott, *J. Appl. Phys.*, 1961, **32**, 1679; (*b*) I. V. Savchenko and S. V. Stankus, *Thermophys. Aeromechanics*, 2008, **15**, 729.

29 J. A. Cape and G. W. Lehman, *J. Appl. Phys.*, 1963, **34**, 1909.

30 J. Blumm and J. Opfermann, *High Temp. – High Pressures*, 2002, **34**, 515.

K. Liu, X. Zou, W. Li, Q. J. Wang and Y. Zhang, *Opt. Lett.*, 2019, **44**, 2422.